Acta Materialia 214 (2021) 116936

Contents lists available at ScienceDirect

Acta Materialia

journal homepage: www.elsevier.com/locate/actamat

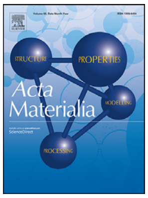

Full length article

A thermal grooving study of relative grain boundary energies of nickel in polycrystalline Ni and in a Ni/YSZ anode measured by atomic force microscopy

Patricia Haremski[a,b,*], Lars Epple[a], Matthias Wieler[a], Piero Lupetin[a], Richard Thelen[c], Michael J. Hoffmann[b]

[a] *Corporate Sector Research and Advance Engineering, Robert Bosch GmbH, Robert-Bosch-Campus 1, 71272 Renningen, Germany*
[b] *Institute of Applied Materials, Karlsruhe Institute of Technology, Haid-und-Neu-Str. 7, 76131 Karlsruhe, Germany*
[c] *Institute of Microstructure Technology, Karlsruhe Institute of Technology, Hermann-von-Helmholtz-Platz 1, 76344 Eggenstein-Leopoldshafen, Germany*

ARTICLE INFO

Article history:
Received 30 October 2020
Revised 8 April 2021
Accepted 24 April 2021
Available online 11 May 2021

Keywords:
Nickel
Grain boundaries (GBs)
Grain boundary energy
Anisotropy
Atomic force microscopy (AFM)

ABSTRACT

Grain boundary grooves of nickel were studied in Ni polycrystals and in Ni/YSZ (nickel/yttria-stabilized zirconia) anode microstructures of an solid oxide fuel cell (SOFC) in order to determine the relative grain boundary energies of nickel. Reliable material parameters are necessary for realistic simulations to model the coarsening of nickel grains in SOFC anodes. However, the reported values in literature do not meet the requirements for accuracy and the experimental conditions differ strongly from the conditions within an anode. In this work, the measurement approach for atomic force microscopy was optimized to ensure the required accuracy in measuring grain boundary grooves; the thermal grooving experiments were performed at $T = 750\,^\circ\mathrm{C}$ in dry and humid atmosphere. The resulting distributions of measured dihedral angles and relative grain boundary energies are identical in the polycrystal and the anode microstructure and are independent of annealing time and humidity. For the first time, precise values of the relative grain boundary energies of nickel are determined with high accuracy under operating conditions of an SOFC anode. The mean value of the relative grain boundary energies $\gamma_{\mathrm{GB}}/\gamma_{\mathrm{S}}$ of nickel is 0.475 ± 0.013 for high-angle grain boundaries, 0.217 ± 0.010 for low-angle grain boundaries, 0.157 ± 0.013 for $\Sigma 3$ grain boundaries and 0.019 ± 0.002 for twin boundaries.

1. Introduction

Solid oxide fuel cells (SOFCs) represent a promising future technology for clean electricity generation. They convert the chemical energy of the fuel directly into electrical energy with higher efficiency and less environmental impact than traditional heat engines. One challenge for a wide commercialization of SOFCs is to overcome degradation processes to guarantee the required lifetime. One of the most dominant degradation mechanisms is the *Coarsening of Nickel Grains* in the Ni/YSZ (nickel/yttria-stabilized zirconia) anode under operating conditions [1–6]. This leads to a reduction of the active triple-phase boundary and to a loss of performance. Our goal is to develop a model for describing coarsening of nickel grains in SOFC anodes by means of large-scale 3D phase-field simulations. The study consists of two parts: In this part, we present the experimental results, the results from phase-field simulations will be published elsewhere [7]. In order to be able to make long-term predictions on anode degradation, reliable material parameters like interfacial energies under realistic operating conditions are necessary to simulate the coarsening of nickel grains quantitatively correctly.

Typical operating conditions of an SOFC anode are in the temperature range of about $600\,^\circ\mathrm{C}$ to $900\,^\circ\mathrm{C}$ under a reducing and humid atmosphere. So far, the reported literature data for nickel interfacial energies does not meet the requirements for reliability and accuracy needed for phase-field simulations. A comprehensive review of literature data for Ni surface energies and Ni grain boundary energies is given in Section S1, supplementary material. Overall, these literature values are evaluated in terms of their reliability from the current state of science. A summary of the litera-

---

* Corresponding author at: Corporate Sector Research and Advance Engineering, Robert Bosch GmbH, Robert-Bosch-Campus 1, 71272 Renningen, Germany.
E-mail address: patricia.haremski@de.bosch.com (P. Haremski).

https://doi.org/10.1016/j.actamat.2021.116936
1359-6454/

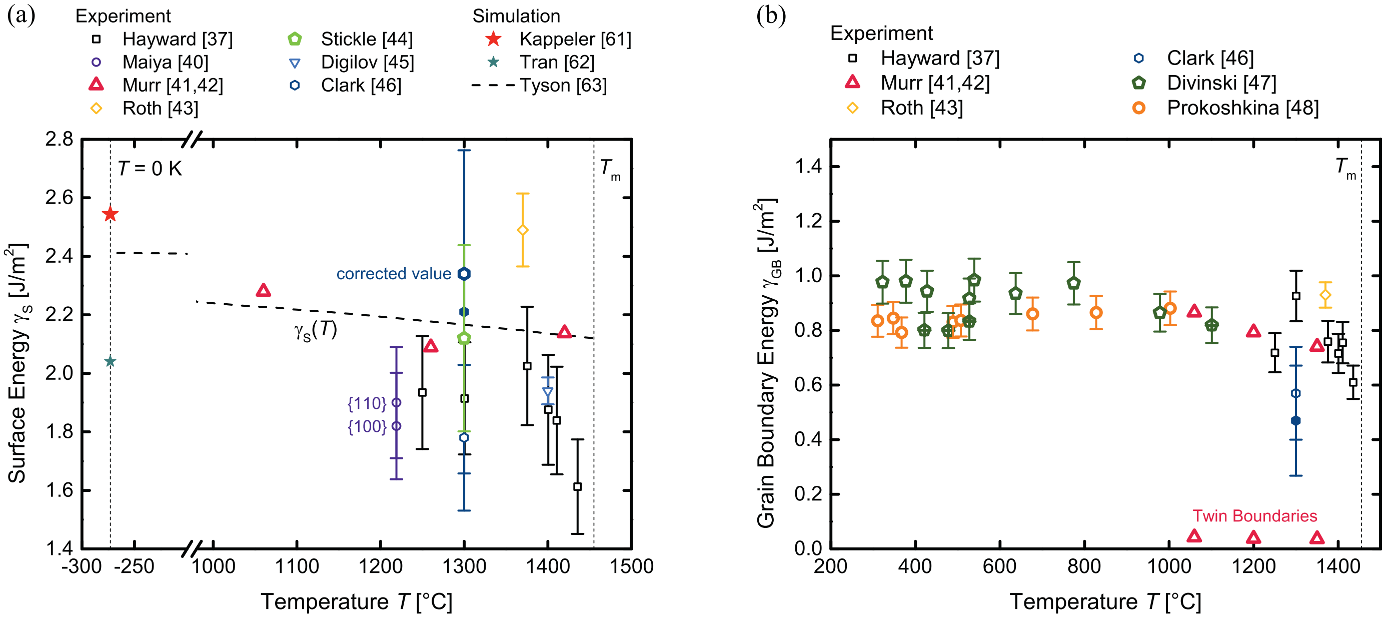

Fig. 1. (a) Mean surface energy γ_S of Ni and (b) mean grain boundary energy γ_{GB} of Ni as a function of temperature. Open symbols: inert atmosphere. Filled symbols: reducing atmosphere. Symbols with a cross: impure Nickel (purity: 99.6 %). The purity of the other Ni samples is > 99.9 %. Star symbols: weighted mean value from atomistic simulations. Literature data evaluated as reliable in this work are highlighted by larger symbols. The zero temperature $T = 0$ K and the melting temperature $T_m = 1455\,^\circ$C of Ni are shown. The references [37,40–48,61–63] are part of this figure.

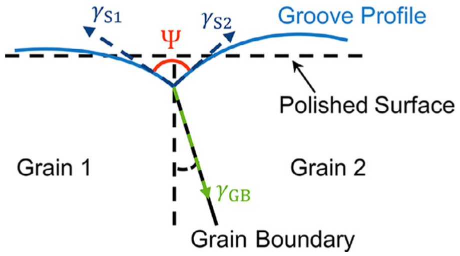

Fig. 2. Sketch of a grain boundary groove. An equilibrium of the interfacial forces has been established locally at the triple point. γ_{S1} and γ_{S2} refer to the surface energies, γ_{GB} to the grain boundary energy and Ψ to the dihedral angle.

ture data of the mean surface energy γ_S and mean grain boundary energy γ_{GB} is given in Table 1 including details about the experimental conditions. In Fig. 1a and b, γ_S and γ_{GB} are shown as a function of temperature, respectively. The experimental conditions differ strongly from the conditions in an SOFC anode and oxygen adsorption which can significantly reduce surface energy cannot be excluded in all cases. The literature values give an initial indication of the order of magnitude of the values, however, they do not achieve the required accuracy and reliability needed for simulations.

For this reason, we performed thermal grooving experiments in this work to determine the relative grain boundary energies of nickel under operating conditions of an SOFC anode and to examine the influence of humidity on this material parameter. *Thermal Grooving* describes the evolution of grain boundary grooves at high temperatures [8–10]. Due to diffusion processes, the grooves evolve in order to equilibrate interfacial forces and to minimize interfacial energies at the groove root (cf. Fig. 2). The general Herring equation [11] describes the relationship between the interfacial geometry and the interfacial energies at a triple line in local equilibrium

$$\gamma_i \boldsymbol{t}_i + \boldsymbol{n}_i \frac{\partial \gamma_i}{\partial \Theta} = 0 \tag{1}$$

whereby γ_i is the energy of the ith interface, $\boldsymbol{t}_i$ and $\boldsymbol{n}_i$ are forces tangential and normal to the interfaces, respectively, and $\frac{\partial \gamma_i}{\partial \Theta}$ describes torque applied to the interfaces. In equilibrium, the six forces must balance and sum to zero. For the case of thermal grooves at surfaces, the Herring equation can be simplified under some assumptions providing the relationship between grain boundary energy γ_{GB} and surface energy γ_S, the so-called relative grain boundary energy γ_{GB}/γ_S [12]:

$$\frac{\gamma_{GB}}{\gamma_S} = 2\cos\left(\frac{\Psi}{2}\right). \tag{2}$$

Thereby, Ψ is the dihedral angle at the groove root (cf. Fig. 2). The following assumptions are made in this equation:

(1) The two surface energies γ_S are equal on either side of the groove root. (2) The grain boundary is perpendicular to the surface. (3) There is no torque applied to the interfaces.

These assumptions are generally not true and therefore, it has to be emphasized that the measurement of a single groove profile is not meaningful. A sufficient amount of grooves has to be measured to characterize the complete distribution — and thus the anisotropy of γ_{GB}/γ_S — as the mean value and width of the distribution are reproducible properties of the sample [10].

So far in literature, mainly ceramic polycrystals were investigated by means of thermal grooving [13–26] as their materialographic preparation is easier compared to metals for this purpose. Thermal grooving studies on metallic samples [27–30] or on bicrystals [31–34] are more limited. Through the development of new measurement methods, the measurement accuracy has been significantly increased over time. In the earliest measurements, the dihedral angle was measured by means of optical interference microscopy [13–20,27]. Later on, metal reference line technique [17,35], scanning electron microscopy with focused ion beam milling [26] or transmission electron microscopy with focused ion beam milling [36] were occasionally used. Nowadays, atomic force microscopy [12,21–25,28–34] is mainly used as this method offers the highest height resolution. In this work, we use the atomic force microscope (AFM) as well and present an optimized measurement approach to minimize the measurement uncertainty.

Table 1
Experimentally determined mean surface energy γ_S and mean grain boundary energy γ_{GB} of Ni from literature.

Ref.	Method	T [°C]	Atmosphere	Purity		γ_S [J/m^2]	Error	γ_{GB} [J/m^2]	Error	γ_{GB}/γ_S	Error	Ψ [°]	# Ψ
[37]	Zero Creep Technique	1250 - 1453	Ar	4N8		1.61 - 2.03	10 %	0.61 - 0.93	10 %	0.37 - 0.48	8 %	152.0 - 158.6	60
[38]	Thermal Grooving & Interferometry	1000	vacuum	4N	twins					0.015	33 %		9
[39]	Thermal Grooving & Interferometry	1300	vacuum	N/A						0.26	13 %	165.0	11
[40]	Surface Relaxation Measurement	1219	vacuum	3N8	{100}	1.82	10 %						
		1219	vacuum	3N8	{110}	1.90	10 %						
[41]	Zero Creep Technique	1060	He	3N7		2.28	N/A	0.866	N/A	0.38	N/A	158	100
		1060	He	3N7	twins			0.043	N/A				
[42]	Zero Creep Technique	1200 - 1420	He	3N7		2.09 - 2.14	N/A	0.74 - 0.79	N/A				
		1200 - 1420	He	3N7	twins			0.037	N/A				
[43]	Zero Creep Technique	1370	He	4N7		2.49	5 %	0.930	5 %	0.37	12 %	158.7	N/A
[44]	Zero Creep Technique	1300	10^{-6} Pa O_2	3N7		2.01	15 %						
		1300	10^{-7} Pa O_2	3N7		1.29	15 %						
		1300	10^{-13} Pa O_2	3N7		2.12	15 %						
		1300	10^{-13}Pa O_2	3N7	foil					0.24	10 %	166.2	N/A
		1300	10^{-13} Pa O_2	3N7	twins					0.012	10 %		
[45]	Compensated Zero Creep Technique	1400	vacuum	5N		1.940	2.5 %						
[46]	Zero Creep Technique	1300	Ar	4N		1.78	14 %	0.57	30 %	0.32	17 %	162	23
						$< 2.34^a$							
		1300	Ar/H_2	4N		2.21	25 %	0.47	42 %	0.21	17 %	167	30
[47]	Radiotracer Technique	320 - 980	Ar	5N				0.86 - 0.98	8 %				
[47]	Radiotracer Technique	420 - 1100	Ar	2N6				0.80 - 0.83	8 %				
[48]	Radiotracer Technique	310 - 1000	Ar	4N				0.79 - 0.88	7 %				

[a] corrected value

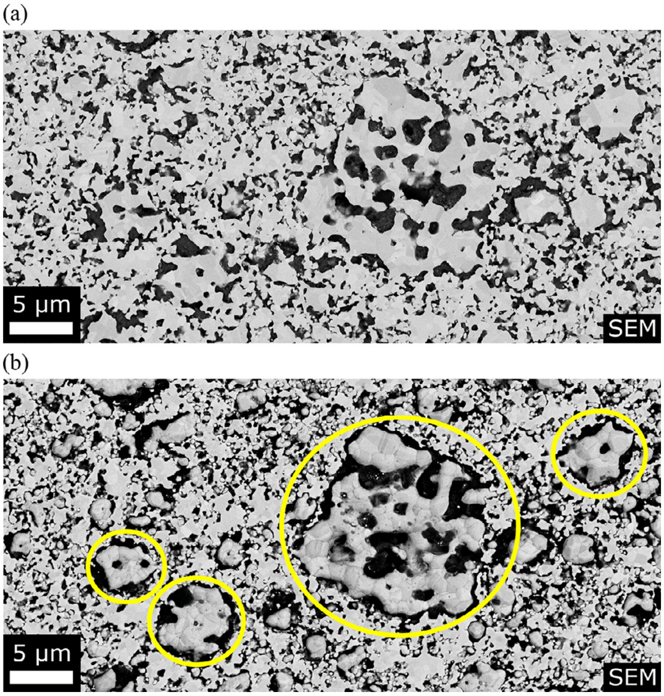

Fig. 3. SEM image (BSE mode) of the anode microstructure (a) as polished before thermal grooving and (b) after thermal grooving (5 h at 750 °C in forming gas). The larger Ni agglomerates can be easily recognized by their rounding (cf. yellow circles). The phase-boundary between the Ni agglomerates and the YSZ on the surface is no longer present.

2. Experimental

2.1. Ni/YSZ anode

Anode symmetric cells build up of anode, electrolyte and anode were used in this work. The cell consists of 20 μm thick Ni/YSZ anodes each and a 200 μm thick YSZ electrolyte and has a diameter of 8 mm. The cell is fabricated by screen printing and lamination of two half cells. The anode paste is composed of NiO powder ($SSA = 8\,m^2/g$) and 8YSZ powder ($SSA = 11\,m^2/g$) mixed with an organic binder, a solvent and further organic additives. The electrolyte paste has the same ingredients except for the NiO powder. After screen printing and lamination under pressure and temperature the cell is thermally debinded and subsequently fired at a temperature between 1150 °C and 1250 °C for 5 h. The reduction of NiO to Ni was carried out according to an in-house reduction scheme at a temperature between 800 °C and 900 °C involving successive replacement of nitrogen with hydrogen, long enough to fully reduce the NiO. The materialographic preparation of the anode surface is summed up in Section S2, supplementary material. Between the individual preparation steps, the samples were thoroughly cleaned using deionized water and ethanol. An SEM image (BSE mode, accelerating voltage: 7 kV) of the polished surface of the anode microstructure is shown in Fig. 3a. Figure 3b shows the same location after thermal grooving (5 h at 750 °C in forming gas). The larger Ni agglomerates can be easily recognized by their rounding which could be proven by energy-dispersive spectroscopy (EDS). It can also be seen that the phase-boundary between the Ni agglomerates and the YSZ on the surface is no longer present.

2.2. Ni polycrystal

A 6.8 mm thick polycrystalline Ni sheet (99.99% Ni, HMW Hauner GmbH & Co. KG) was cross-rolled to 0.5 mm thickness.

The cold-worked sheet was then vacuum-annealed at 400 °C for 1 h which lead to a full recrystallization of the microstructure with an average grain diameter of 30 μm and sectioned in 5 mm × 5 mm samples. The polycrystalline samples were one-sided polished by chemical-mechanical polishing (MaTecK GmbH). Prior to thermal grooving, ion beam flat milling (accelerating voltage: 2 kV, tilt: 10 °, rotation speed: 25 r/min, time: 2 min) was applied using a Hitachi IM4000Plus Ar ion milling system (Hitachi High-Technologies Corporation) to produce a smooth and clean crystalline surface suitable for electron backscatter diffraction (EBSD).

2.3. Thermal grooving

Thermal grooving was carried out in a tube furnace (HTM Reetz GmbH) inside an aluminium-oxide tube under constant gas flow. As we are interested in material parameters under operating conditions of an SOFC anode, the temperature $T = 750\,^{\circ}$C and a reducing atmosphere were chosen. The carrier gas was forming gas (95 % N_2/5 % H_2, flow rate: 1.0 l/min). The furnace was heated up with a rate of 10 K/min. Cooling followed an exponential change in temperature as the furnace could only be cooled down slowly.

Three identical anode microstructures at different annealing times ($t = 0.5$ h, 5 h, 100 h) were investigated to check whether an equilibrium at the groove root was already locally established after the shortest selected annealing time. The influence of humidity was investigated on the polycrystalline samples, since in comparison to the anode microstructure the dihedral angle could be determined with greater accuracy in polycrystals. A maximum humid atmosphere (29 vol.% H_2O and 71 vol.% forming gas) was chosen, which is possible with this experimental setup and the utilized gas connections, without annealing in an oxidizing atmosphere. This corresponds to a ratio $H_2/H_2O = 0.12$. The measured oxygen partial pressure in dry forming gas was $p_{O_2} = 10^{-25}$ atm and in humid forming gas $p_{O_2} = 10^{-19}$ atm. To generate a humid atmosphere, water was evaporated by means of a CEM system (Controlled Evaporation Mixing) from Bronkhorst (Schweiz) AG and mixed with forming gas at temperatures $T > 150\,^{\circ}$C. The flow rate of H_2O was 10.0 g/h, the flow rate of forming gas was 0.5 l/min. After annealing ($t = 27$ h), EBSD measurements were performed on both polycrystalline samples to distinguish between different types of grain boundaries: Σ3-GBs, general HAGBs (excluding Σ3-GBs) and LAGBs. The EBSD analysis was carried out in the SEM Supra 55VP (Carl Zeiss AG) equipped with the EBSD system AZtec (Channel 5, Oxford Instruments) operating at an accelerating voltage of 20 kV. A 3 mm × 3 mm large field with a step width of 0.75 μm was measured. The MAD (mean angle deviation) value was 0.25. The proportion of the distinct grain boundaries in the total grain boundary length was 45 % for Σ3-GBs, 45 % for HAGBs and 10 % for LAGBs.

2.4. Atomic force microscopy

Atomic force microscopy was used in tapping mode to measure the groove geometry. The measurements on the anode microstructure were performed using a Dimension 3100 AFM (Veeco Instruments Inc.) and OTESPA tips from Bruker Corporation (tip radius of 7 – 10 nm), the ones on the Ni polycrystals were performed using the Dimension Icon AFM (Bruker Corporation) with SuperSharpStandard-NCHR tips (nanotools GmbH) with a radius of 2 – 3 nm. The evaluation software Gwyddion was used in this work [49].

The accuracy in measuring the geometric profile and thus in determing Ψ is of particular importance as the error propagates calculating γ_{GB}/γ_S. Although the measurement principle of an AFM—the measurement of the topography—seems relatively simple, some issues have to be considered during practical realization [12,21–25,28–34]. The wear of the AFM tip and the influence of the tip shape, non-optimized parameters during measurement and further measurement artefacts can lead to a distorted image. Subsequent image processing can also lead to a modified topography. As the geometric shape of groove profiles is crucial for further evaluation and for determination of γ_{GB}/γ_S, the aforementioned experimental factors and the approach to minimize their impact on measurement accuracy are discussed in detail in Section S3, supplementary material.

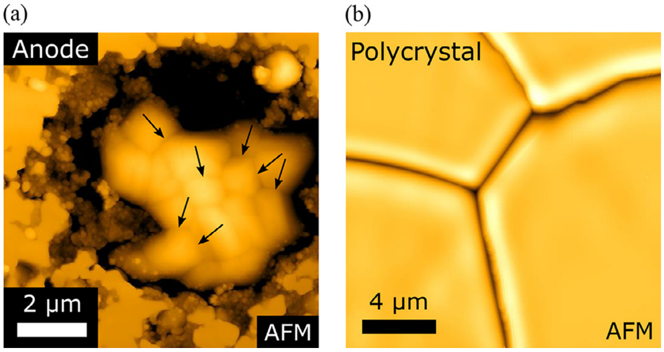

Fig. 4. AFM image of a thermally grooved (a) anode microstructure and (b) Ni polycrystal. Figure (a) shows a larger Ni agglomerate with black arrows indicating some of the grooves. During annealing the Ni grains get strongly rounded and partially detach from the YSZ structure. In comparison, the Ni polycrystal in figure (b) shows significantly larger grains and distinct grooves.

3. Results

3.1. Measurement of dihedral angles

AFM images of a thermally grooved anode microstructure and Ni polycrystal are illustrated in Fig. 4. The samples not only show differences in microstructure, but also in the grooves to be measured. A larger Ni agglomerate in the anode microstructure is visible in Fig. 4a. The anode is porous and has relatively small Ni grains with a diameter < 1 μm. As a result, the Ni grains on the surface get strongly rounded during annealing and the Ni agglomerates protrude a total of 50 – 200 nm compared to the polished surface. Black arrows indicate some of the grooves for better visualization. Due to the small grains and their rounding, the grooves are only slightly pronounced. In comparison to the anode microstructure, the Ni polycrystal is dense, has large grains and well-pronounced, wide grooves (cf. Fig. 4b). During annealing grooves are formed along the complete grain boundaries while the remaining surface of the grains is not rounded.

The grooves to be measured are randomly selected and along a grain boundary the location for AFM acquisition is always selected centrally between the triple points. The approach to determine the dihedral angle Ψ is shown in Fig. 5. High-resolution AFM measurements are performed at the groove root, as shown in Fig. 5a exemplary for a HAGB in the polycrystal. In addition to the high lateral and vertical resolution of the AFM, a further advantage is that not only individual line profiles are evaluated, but they can be averaged over the entire AFM image. Within the rectangle drawn in Fig. 5a, the line profiles are extracted perpendicularly to the grain boundary — in x-direction — as shown in Fig. 5b, and then averaged in y-direction. For the polycrystalline samples, 128 line profiles are always averaged, whereas for the anode microstructure only 8 – 32 line profiles can be averaged due to the rounding of the Ni grains. The averaged profile is shown in Fig. 5c. With increasing distance to the groove root, the absolute value of the slope of the line profile decreases continuously. A linear fit is performed on both sides of the groove root and the dihedral an-

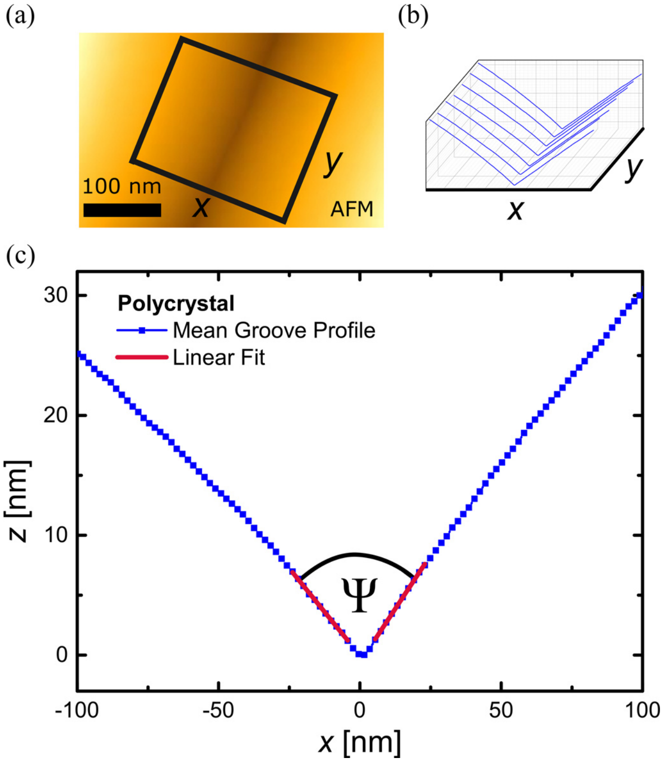

Fig. 5. Approach to determine the dihedral angle Ψ: (a) High-resolution AFM measurement at the groove root, exemplary for a HAGB in the polycrystal. Within the rectangle, the line profiles are extracted perpendicularly to the grain boundary (in *x*-direction) as shown in (b). The line profiles are averaged in *y*-direction and the mean profile in (c) is used to determine Ψ.

gle is calculated as the difference of both slopes. The fit is always performed close to the groove root in the linear inclination range. The coefficient of determination of the linear regression was always $R^2 > 99.5\,\%$ which corresponds to a high goodness of fit.

3.2. Measurement accuracy

Taking into account the optimized measurement approach of AFM as described in Section S3, supplementary material, the actual measurement uncertainty — first for the Ni polycrystal — is to be estimated in the following. On the one hand, the accuracy of the measured topography, which can be distorted by noise of the AFM and by the influence of the AFM tip, and on the other hand, the measurement uncertainty due to the fit process are discussed.

The noise floor in the z piezo signal was determined by AFM measurements on highly oriented pyrolytic graphite (HOPG) and is 75 pm for the AFM Dimension Icon. Using a false engagement, the electronic noise could be measured and was 15 pm. Overall, the system noise of the AFM Dimension Icon is $< 100\,\text{pm}$ and thus is negligible. The necessary quality is achieved to measure the geometry of the groove profiles with sufficient accuracy.

The models discussed in literature to determine the influence of the tip on the measurement uncertainty of dihedral angles are used to estimate the maximum error [12,17,22,26,50,51]. A maximum pessimistic groove geometry is assumed which could occur within these polycrystals — a narrow groove profile with a width of $w = 1\,\mu\text{m}$ and a dihedral angle of $\Psi = 130^\circ$. The SuperSharpStandard-NCHR tips used in these measurements are specified with a tip radius of $2 - 3$ nm. According to the models, this results in a maximum measurement uncertainty of $\Delta\Psi = 0.07^\circ$ whereby it has to be emphasized that this corresponds to the maximum estimate and that the measurement uncertainty due to the tip shape will generally be smaller. Thus there is no systematic overestimation of the dihedral angle as in the above-mentioned literature sources. In summary, it can be concluded that HDC/DLC tips according to the current state-of-the-art enable an accuracy in AFM measurements of groove profiles that was not possible in earlier publications.

The selection of the linear inclination range during the fit process influences the slope and thus the value of the dihedral angle. A high lateral resolution during measurement ensures enough data points for a fit. In the case of the polycrystals, the lateral resolution was 1 nm. To estimate the measurement uncertainty due to the fit process, the linear inclination range was varied to determine the minimum and maximum slope which was still acceptable (cf. Section S4, supplementary material). The maximum measurement uncertainty of Ψ due to the fit process can be stated with $\Delta\Psi = 0.2^\circ$.

To sum up, the influence of the noise of the AFM and the influence of the AFM tip on the accuracy of the dihedral angle Ψ in the polycrystal are negligible. The measurement uncertainty is dominated by the fit process and can be specified as $\Delta\Psi = 0.2^\circ$ for the polycrystals. Considering the factors mentioned above a maximum measurement uncertainty $\Delta\Psi = 1.8^\circ$ is obtained for the anode samples. The larger measurement uncertainty compared to the polycrystals is mainly due to the rounding of the grains and the weakly pronounced grooves as well as due to the lower lateral resolution (10 nm) of the AFM Dimension 3100.

3.3. Measured dihedral angles

23 to 25 dihedral angles per anode sample were measured to investigate the influence of annealing time. EBSD images were taken of the Ni polycrystals to distinguish between HAGBs, LAGBs and Σ3-GBs and about 50 dihedral angles were measured for each grain boundary type in dry and humid atmosphere. The descriptive statistics for the distributions of measured dihedral angles are summarized in Table 2.

4. Discussion

4.1. Influence of annealing time

In the case of the anode samples, the Mann-Whitney *U* test reveals that there are no statistically significant differences between the distributions of dihedral angles (cf. Section S5, supplementary material) and that they can be considered as distributions of the same population independent of annealing time. This has also been shown for other materials in literature [15,19,20]. Thus, the three data sets of the anode samples can be combined into one data set representing the distribution of the dihedral angles in the anode microstructure.

4.2. Influence of microstructure

The data sets of the anode microstructure and the Ni polycrystal in forming gas are compared in order to investigate if there are any differences in the distributions of dihedral angles and thus in the relative grain boundary energies. The cumulative distributions of dihedral angles for both microstructures are shown in Fig. 6. The distributions in the Ni polycrystal show clear differences between the different grain boundary types. The distributions of the LAGBs and the Σ3-GBs are shifted to higher dihedral angles compared to the distribution of the HAGBs. These grain boundary grooves are flatter and more difficult to locate in the AFM. The distribution of the anode nearly follows the distribution of the HAGBs in the polycrystal. They show a significant consistency in the range between 130° and 150°. For dihedral angles $\Psi > 150^\circ$ the distribution of

Table 2
Descriptive statistics on the measured dihedral angles of the anode samples and of the Ni polycrystals in dry and humid forming gas. The samples were annealed at $T = 750\,^{\circ}$C. SE refers to the standard error of mean and σ to the standard deviation.

				$\Psi[^{\circ}]$					
	$t[h]$	Forming gas	Number	Mean value	SE	σ	Median	Min	Max
Anode I	0.5	dry	23	151.3	1.2	5.8	152.4	141.6	160.8
Anode II	5	dry	25	149.8	1.4	7.2	150.0	135.8	164.1
Anode III	100	dry	24	152.5	1.6	7.9	152.0	136.3	168.0
Polycrystal - HAGB	27	dry	54	152.4	1.1	7.8	151.7	134.3	167.1
		humid	53	152.6	1.1	8.0	151.5	138.1	172.5
Polycrystal - LAGB	27	dry	50	168.3	0.8	5.6	168.9	155.1	179.1
		humid	48	166.7	0.9	6.1	166.8	153.8	179.1
Polycrystal - Σ3-GB	27	dry	47	171.7	1.1	7.3	174.3	146.8	179.1
		humid	53	170.3	1.1	8.0	172.6	147.8	179.5

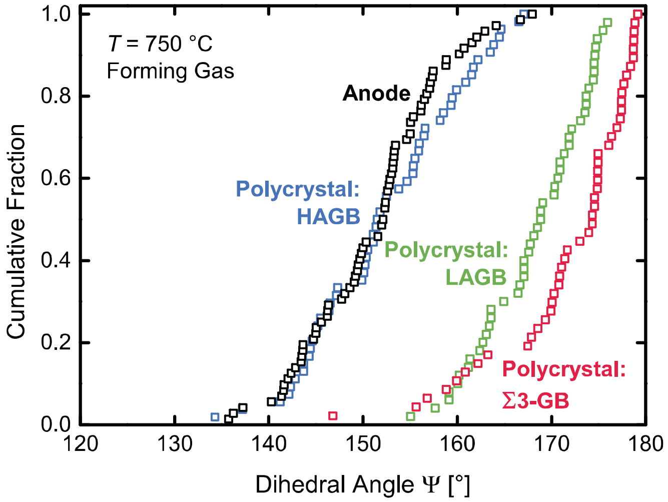

Fig. 6. Cumulative distributions of dihedral angles Ψ for the anode microstructure and the Ni polycrystal, the latter distinguished between HAGB, LAGB and Σ3-GB, annealed at $T = 750\,^{\circ}$C in dry forming gas.

the anode is slightly above the distribution of the HAGBs. From the comparison of anode and polycrystal in this diagram the hypothesis can be made that the distributions of dihedral angles of nickel are identical in both microstructures and that in comparison to the polycrystal in the anode sample the complete population was not measured. Due to the rounding of the small Ni grains and the resulting weakly pronounced grooves in the anode microstructure, only grooves with $\Psi < 170^{\circ}$ could be located and measured in the AFM. In the range between 130° and 150° only high-angle grain boundaries were measured in the polycrystal. Due to the good accordance of distributions in this area it can be concluded that in the anode microstructure as well only high-angle grain boundaries were measured. The course for $\Psi > 150^{\circ}$ in the anode can be explained by the fact that in addition to the HAGBs, some low-angle and Σ3 grain boundaries were also measured. Therefore, the distribution of the anode is above the distribution of pure HAGBs in this area. In summary, it was not possible to represent the complete population of dihedral angles in the anode microstructure, however, it is conclusive that the distributions of dihedral angles, and thus the relative grain boundary energies, are identical in both microstructures. For further analysis, the Ni polycrystal is considered as the complete population of dihedral angles can be measured for different grain boundary types in nickel.

4.3. Influence of humidity

To investigate the influence of humidity on the relative grain boundary energy, the dihedral angles Ψ of the Ni polycrystals in dry and humid atmosphere are compared. The distributions for HAGBs, LAGBs and the Σ3-GBs are regarded separately and the Mann-Whitney *U* test is performed for each grain boundary type. The details for the calculation of the test can be found in Section S4, supplementary material. The cumulative distributions of dihedral angles — divided by grain boundary type — are shown in Fig. 7. In the upper diagram, the distributions for HAGBs show a significant consistency. This is also confirmed by the Mann-Whitney *U* test. The distributions for LAGBs, which are shown in the middle diagram, exhibit similar characteristics in both atmospheres, whereby the distribution in humid atmosphere is shifted slightly to lower dihedral angles compared to that in dry atmosphere (see also the mean values in the diagram). However, the Mann-Whitney *U* test reveals that no significant difference can be assumed. The proportion of LAGBs at all grain boundaries is comparatively low and amounts to 10 %. The LAGBs, which were identified in the EBSD images, occurred mainly in clusters and all LAGBs occurring in the images were measured by AFM. The difference between the distributions in dry and humid atmosphere can be explained by the fact that the LAGBs were not sufficiently representative and in both cases the complete population could not be represented. The cumulative distributions of dihedral angles for the Σ3-GBs in the lower graph show an exponential behavior and are in good agreement. The Mann-Whitney *U* test confirms that there is no significant difference between dry and humid atmosphere.

It can be stated that the distributions of dihedral angles in dry and humid atmosphere do not show any significant difference for the three grain boundary types and that they can be considered as distributions of the same population independent of humidity. Since the relative grain boundary energy $\gamma_{\mathrm{GB}}/\gamma_{\mathrm{S}}$ follows from the dihedral angle Ψ with Eq. (2), it can be concluded that humidity under these annealing conditions[1] has no influence on the relative grain boundary energy. The oxygen partial pressure was $p_{\mathrm{O}_2} = 10^{-25}$ atm in dry forming gas. The proportion of H_2O in the gas mixture increased the oxygen partial pressure to $p_{\mathrm{O}_2} = 10^{-19}$ atm. According to the Ellingham diagram [52,53] this value was still low enough and there was no oxidizing atmosphere. Thus, no oxygen was adsorbed on the surface which could lower the surface energy γ_{S}.

As the distributions of dihedral angles and thus of the relative grain boundary energies are independent of humidity, the data sets in dry and humid atmosphere are merged, for further evaluation, to one data set each representing the distribution of dihedral angles of nickel for HAGBs, LAGBs and Σ3-GBs in reducing atmosphere.

---

[1] 29 vol.% H_2O / 71 vol.% forming gas at $T = 750\,^{\circ}$C

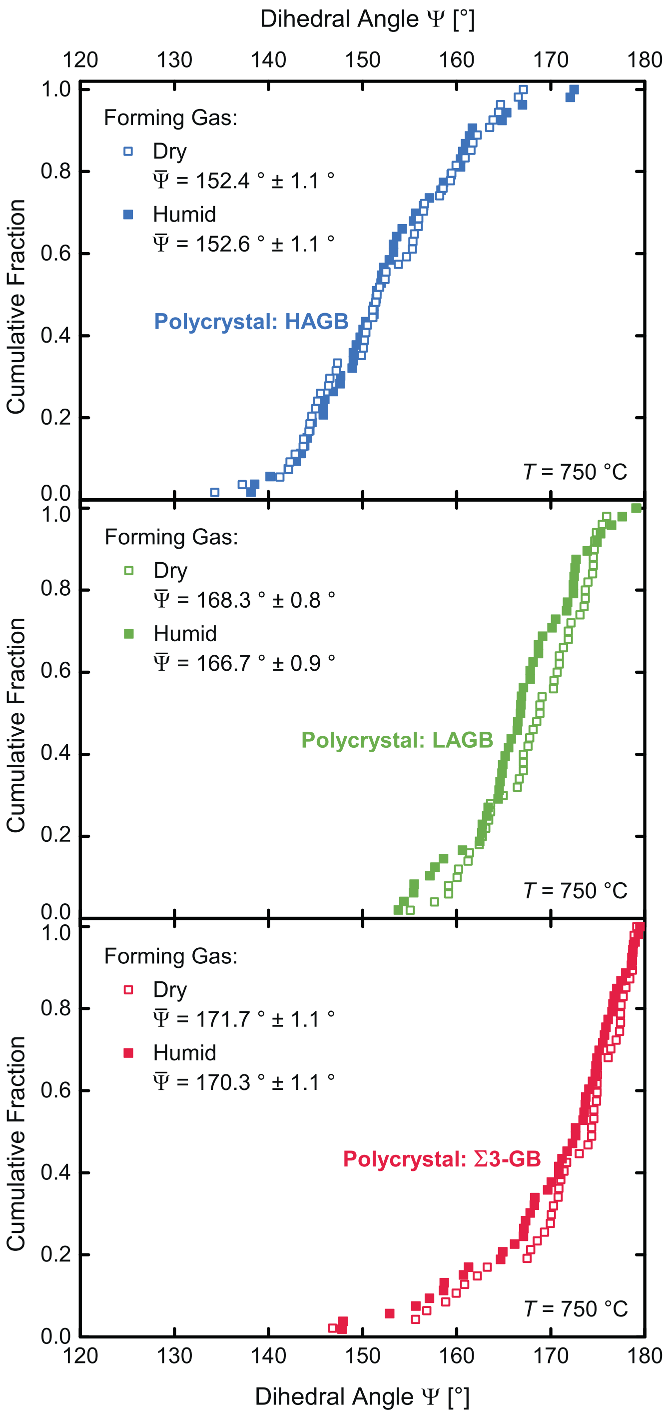

Fig. 7. Cumulative distributions of dihedral angles Ψ for the Ni polycrystals in dry and humid forming gas at $T = 750\,^\circ$C. The mean value $\bar{\Psi}$ of each distribution and the standard error of mean are given in the diagram.

4.4. Relative grain boundary energy

The relative grain boundary energy γ_{GB}/γ_S is calculated with Eq. (2) for each dihedral angle Ψ. Using error propagation, the error for a single data point can be calculated to $\Delta(\gamma_{GB}/\gamma_S) = 0.003$. In Fig. 8 the cumulative distributions of the relative grain boundary energies of nickel at $T = 750\,^\circ$C in reducing atmosphere are shown and the mean values are summarized in Table 3. The distributions are independent of annealing time and humidity. A different representation of the data is shown in Fig. 9a as box plots. It is noticeable that the distributions are in general broad and range in total from 0 to 0.8. This wide variation can be attributed mainly to the anisotropy of the grain boundary energies. Σ3-GBs and LAGBs are lower in energy than general HAGBs and the energy of LAGBs approaches the value zero for small misorientations which is both consistent with literature [54–59]. In the main, Σ3-GBs are frequently represented in nickel and comprise about 45 % of the total grain boundary length which was also observed in the work of Randle[54], [56] and Rohrer et al. (40 %) [60]. The distribution for Σ3-GBs shows an exponential behavior in the cumulative fraction with low-energy grain boundaries occurring most frequently (cf. Fig. 8) which is also consistent with the results of Rohrer et al. [60]. The Σ3-GBs can be distinguished in coherent twin boundaries and incoherent Σ3-GBs. The coherent twin has the lowest grain boundary energy whereas the grain boundary energies of incoherent Σ3-GBs are higher and vary strongly [58–60]. To determine the relative grain boundary energy of the twin boundary from our data we take the mean value of the 10 lowest data points which are almost on top of each other in the cumulative distribution plot (cf. Fig. 8). The relative grain boundary energy of the coherent twin can be stated to $\gamma_{GB}/\gamma_S = 0.019 \pm 0.002$.

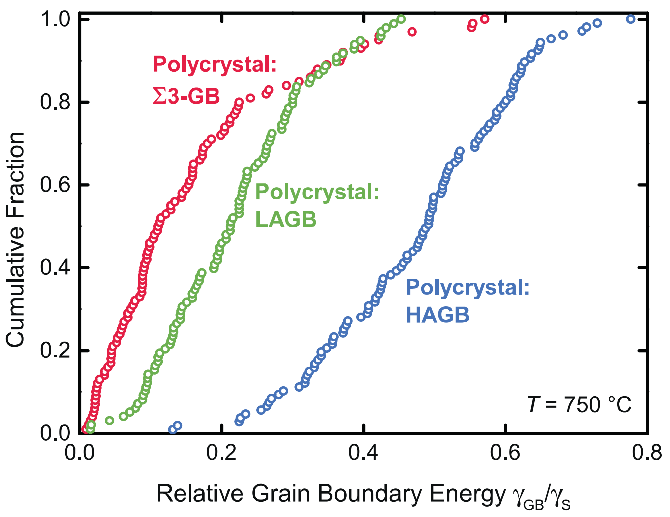

Fig. 8. Cumulative distributions of relative grain boundary energies γ_{GB}/γ_S of Ni for HAGBs, LAGBs and Σ3-GBs at $T = 750\,^\circ$C.

Table 3
Mean value of dihedral angles Ψ and the relative grain boundary energies γ_{GB}/γ_S in nickel at $T = 750\,^\circ$C. SE refers to the standard error of mean and σ to the standard deviation.

		Ψ[°]		γ_{GB}/γ_S		
	Number	Mean value	SE	Mean value	SE	σ
HAGB	107	152.5	0.8	0.475	0.013	0.133
LAGB	98	167.5	0.6	0.217	0.010	0.102
Σ3-GB	100	171.0	0.8	0.157	0.013	0.132

To compare the measured values with literature data, the mean value is used and plotted in Fig. 9b. In most literature sources no distinction was made between different types of grain boundaries. In addition, the relative grain boundary energy determined by Hayward and Greenough [37] and Clark et al. (in inert atmosphere) [46] are less reliable as oxygen adsorption cannot be excluded. The value from Clark et al. in reducing atmosphere [46] is decreased due to hydrogen dissolved in nickel. In the work of Williams and Barrand [39] and Stickle et al. [44] Ni foils were used exhibiting texture which decreased the relative grain boundary energy. The relative grain boundary energy determined by Murr et al. [41] and the one determined by Roth [43] as well as the values for twin

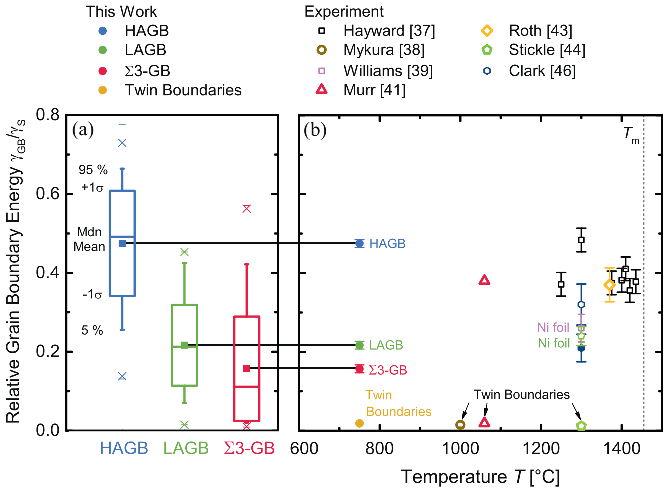

Fig. 9. (a) Box plot of distributions of relative grain boundary energies of Ni for HAGBs, LAGBs and Σ3-GBs at $T = 750\,^{\circ}\mathrm{C}$. (b) Mean relative grain boundary energy γ_{GB}/γ_S of Ni as a function of temperature. Open symbols: inert atmosphere. Filled symbols: reducing atmosphere. Literature data evaluated as reliable in this work are highlighted by larger symbols. The melting temperature $T_m = 1455\,^{\circ}\mathrm{C}$ of Ni is shown.

boundaries [38,41,44] can be considered reliable. Murr et al. distinguished between twin boundaries and high-angle grain boundaries. However, the high-angle grain boundaries included incoherent Σ3-GBs in contrast to our work. The same applies to the work of Roth. Thus, their values are between the relative grain boundary energy for HAGBs and the one for Σ3-GBs from this work. The twin boundaries are most suitable as reference and the value determined in this work fits well to the reported values in literature.

As the grain boundary energy varies more than the surface energy for different orientations, a mean value of the surface energy can be taken to determine the grain boundary energy from our data. Assuming $\gamma_S(T = 750\,^{\circ}\mathrm{C}) = 2.29$ J/m^2 from the estimation of $\gamma_S(T)$ in Fig. 1a results in mean grain boundary energies of (1.09 ± 0.08) J/m^2 for HAGBs, (0.50 ± 0.04) J/m^2 for LAGBs, (0.36 ± 0.03) J/m^2 for Σ3-GBs and (0.044 ± 0.006) J/m^2 for twin boundaries. The stated errors refer to the standard error of mean. The mean values for HAGBs and twin boundaries can be compared with the reliable literature data in Fig. 1b. The mean grain boundary energy for twin boundaries is consistent with the values determined by Murr et al. [41], Murr [42] ranging from 0.036 J/m^2 to 0.043 J/m^2. The mean grain boundary energy for HAGBs is slightly higher than the values determined by Divinski et al. [47], Prokoshkina et al. [48] and Murr et al. [41], Murr [42] due to the fact that the high-angle grain boundaries in literature included incoherent Σ3-GBs as well, reducing the mean grain boundary energy.

Considering the wide anisotropy of grain boundary energy in this work, it ranges from 0.30 J/m^2 to 1.78 J/m^2 for HAGBs, from 0.03 J/m^2 to 1.04 J/m^2 for LAGBs and from 0.02 J/m^2 to 1.31 J/m^2 for Σ3-GBs. These energy ranges are in good accordance with the simulation results for $T = 0$ K from Olmsted et al. [59] which show a wide variation of grain boundary energy for different grain boundary types as well.

5. Conclusions

The aim of this work was to determine the relative grain boundary energies of nickel under operating conditions of an SOFC anode. Reliable values are necessary for simulations in order to model the coarsening of nickel grains quantitatively correctly and to be able to make long-term predictions on anode degradation. However, the reported values in literature do not meet the requirements for accuracy and, in addition, the experimental conditions differed strongly from the conditions within an SOFC anode. In this work, thermal grooving experiments were performed on Ni polycrystals and Ni/YSZ anode microstructures at $T = 750\,^{\circ}\mathrm{C}$ in dry and humid forming gas and the groove profiles were measured by means of atomic force microscopy. In combination with the optimized measurement approach of AFM as presented in this work, thermal grooving allows a high measurement accuracy in measuring the groove profile and thus in determining the dihedral angle and the relative grain boundary energy.

It can be concluded that the distributions of dihedral angles and relative grain boundary energies for Ni are identical in polycristalline Ni and the Ni/YSZ anode and that they are independent of annealing time and humidity. The distributions are in general broad and the mean value of the relative grain boundary energies γ_{GB}/γ_S is 0.475 ± 0.013 for high-angle grain boundaries, 0.217 ± 0.010 for low-angle grain boundaries, 0.157 ± 0.013 for Σ3 grain boundaries and 0.019 ± 0.002 for twin boundaries. These results complement the experimental and simulative work done so far in literature and they give for the first time precise values of relative grain boundary energies of nickel under operating conditions of an SOFC anode which can be used with confidence by material scientists in simulations.

Declaration of Competing Interest

The authors declare that they have no known competing financial interests or personal relationships that could have appeared to influence the work reported in this paper.

Acknowledgements

This work was supported by the German Federal Ministry for Economic Affairs and Energy (BMWi) within the project KerSOLife100 (FKZ: 03ET6101A). This work was partly carried out with the support of the Karlsruhe Nano Micro Facility (KNMF, www.kit.edu/knmf), a Helmholtz Research Infrastructure at Karlsruhe Institute of Technology (KIT, www.kit.edu). The first author thanks Paul Hoffrogge and Daniel Schneider from Karlsruhe Institute of Technology, Prof. Gregory Rohrer from Carnegie Mellon University and Prof. Eugen Rabkin from Technion for many interesting discussions.

Supplementary material

Supplementary material associated with this article can be found, in the online version, at doi:10.1016/j.actamat.2021.116936.

References

[1] N. Brandon, E. Ruiz-Trejo, P. Boldrin, Solid Oxide Fuel Cell Lifetime and Reliability: Critical Challenges in Fuel Cells, Elsevier Science, Amsterdam, 2017.
[2] M.S. Khan, S.B. Lee, R.H. Song, J.W. Lee, T.H. Lim, S.J. Park, Fundamental mechanisms involved in the degradation of nickel-yttria stabilized zirconia (Ni-YSZ) anode during solid oxide fuel cells operation: a review, Ceram. Int. 42 (2015) 35–48.
[3] M. Trini, A. Hauch, S. De Angelis, X. Tong, P.V. Hendriksen, M. Chen, Comparison of microstructural evolution of fuel electrodes in solid oxide fuel cells and electrolysis cells, J. Power Sources 450 (2020) 227599.
[4] P. Tanasini, M. Cannarozzo, P. Costamagna, A. Faes, J.V. Herle, C. Comninellis, Experimental and theoretical investigation of degradation mechanisms by particle coarsening in SOFC electrodes, Fuel Cells 9 (2009) 740–752.
[5] D. Kennouche, Y.-C.K. Chen-Wiegart, J.S. Cronin, J. Wang, S.A. Barnett, Three-dimensional microstructural evolution of Ni-yttria-stabilized zirconia solid oxide fuel cell anodes at elevated temperatures, J. Electrochem. Soc. 160 (2013) 1293–1304.
[6] J.-H. Lee, H. Moon, H.-W. Lee, J. Kim, J.-D. Kim, K.-H. Yoon, Quantitative analysis of microstructure and its related electrical property of SOFC anode, Ni-YSZ cermet, Solid State Ion. 148 (2002) 15–26.

[7] P. Hoffrogge, et al., in preparation.
[8] W.W. Mullins, Theory of thermal grooving, J. Appl. Phys. 28 (1957) 333–339.
[9] W. Mullins, Grain boundary grooving by volume diffusion, Trans. Metall. Soc. AIME 218 (1960) 354–361.
[10] W.M. Robertson, Grain-boundary grooving by surface diffusion for finite surface slopes, J. Appl. Phys. 42 (1971) 463–467.
[11] C. Herring, Some theorems on the free energies of crystal surfaces, Phys. Rev. 82 (1951) 87–93.
[12] D.M. Saylor, G.S. Rohrer, Measuring the influence of grain-boundary misorientation on thermal groove geometry in ceramic polycrystals, J. Am. Ceram. Soc. 82 (1999) 1529–1536.
[13] E. Hodkin, M. Nicholas, Surface and interfacial properties of stoichiometric uranium dioxide, J. Nucl. Mater. 47 (1973) 23–30.
[14] P. Nikolopoulos, S. Nazaré, F. Thümmler, Surface, grain boundary and interfacial energies in UO_2 and UO_2-Ni, J. Nucl. Mater. 71 (1977) 89–94.
[15] P. Nikolopoulos, Surface, grain-boundary and interfacial energies in Al_2O_3 and Al_2O_3-Sn, Al_2O_3-Co systems, J. Mater. Sci. 20 (1985) 3993–4000.
[16] A.R. Gaddipati, W.D. Scott, Surface mass transport of alumina, J. Mater. Sci. 21 (1986) 419–423.
[17] C.A. Handwerker, J.M. Dynys, R.M. Cannon, R.L. Coble, Metal reference line technique for obtaining dihedral angles from surface thermal grooves, J. Am. Ceram. Soc. 73 (1990) 1365–1370.
[18] A. Tsoga, P. Nikolopoulos, Groove angles and surface mass transport in polycrystalline alumina, J. Am. Ceram. Soc. 77 (1994) 954–960.
[19] N. Zouvelou, X. Mantzouris, P. Nikolopoulos, Surface and grain-boundary energies as well as surface mass transport in polycrystalline CeO_2, Mater. Sci. Eng. A 495 (2008) 54–59.
[20] G. Triantafyllou, G.N. Angelopoulos, P. Nikolopoulos, Surface and grain-boundary energies as well as surface mass transport in polycrystalline yttrium oxide, J. Mater. Sci. 45 (2010) 2015–2022.
[21] W. Shin, W.-S. Seo, K. Koumoto, Grain-boundary grooves and surface diffusion in polycrystalline alumina measured by atomic force microscope, J. Eur. Ceram. Soc. 18 (1998) 595–600.
[22] E. Saiz, R.M. Cannon, A.P. Tomsia, Enhanced atomic transport at liquid metal/Al_2O_3 interfaces, Acta Metall. 47 (1999) 4209–4220.
[23] M. Jin, E. Shimada, Y. Ikuma, Atomic force microscopy study of surface diffusion in polycrystalline CeO_2 via grain boundary grooving, J. Ceram. Soc. Japan 108 (2000) 456–461.
[24] S. Bhowmick, J.L. Riesterer, Y. Xue, C.B. Carter, Phase-boundary grooving at surfaces of solid oxide fuel cell materials, in: N.P. Bansal, P. Singh (Eds.), Advances in Solid Oxide Fuel Cells V, John Wiley & Sons, Hoboken (NJ), 2009, pp. 105–112.
[25] M.N. Kelly, S.A. Bojarski, G.S. Rohrer, The temperature dependence of the relative grain-boundary energy of yttria-doped alumina, J. Am. Ceram. Soc. 100 (2017) 783–791.
[26] N. Ni, Y. Kaufmann, W.D. Kaplan, E. Saiz, Interfacial energies and mass transport in the Ni(Al)-Al_2O_3 system: the implication of very low oxygen activities, Acta Mater. 64 (2014) 282–296.
[27] G.E. Rhead, Surface self-diffusion and faceting on silver, Acta Metall. 11 (1963) 1035–1042.
[28] P. Sachenko, Experimental and simulated grain boundary groove profiles in tungsten, Philos. Mag. Lett. 80 (2000) 627–631.
[29] E. Rabkin, L. Klinger, The fascination of grain boundary grooves, Mater. Sci. Technol. 17 (2001) 772–776.
[30] Y. Amouyal, E. Rabkin, A scanning force microscopy study of grain boundary energy in copper subjected to equal channel angular pressing, Acta Mater. 55 (2007) 6681–6689.
[31] M. Jin, E. Shimada, Y. Ikuma, Grain boundary grooving by surface diffusion in $SrTiO_3$ Bicrystal, J. Mater. Res. 14 (1999) 2548–2553.
[32] M.I. Peters, I.E. Reimanis, Grain boundary grooving studies of yttrium aluminum garnet (YAG) bicrystals, J. Am. Ceram. Soc. 86 (2003) 870–872.
[33] H. Nishimura, K. Matsunaga, T. Saito, T. Yamamoto, Y. Ikuhara, Atomic structures and energies of $\Sigma 7$ symmetrical tilt grain boundaries in alumina bicrystals, J. Am. Ceram. Soc. 86 (2003) 574–580.
[34] E. Rabkin, A. Gabelev, L. Klinger, V.N. Semenov, S.I. Bozhko, Grain boundary grooving in molybdenum bicrystals, J. Mater. Sci. 41 (2006) 5151–5160.
[35] C.A. Handwerker, J.M. Dynys, R.M. Cannon, R.L. Coble, Dihedral angles in magnesia and alumina: distributions from surface thermal grooves, J. Am. Ceram. Soc. 73 (1990) 1371–1377.
[36] Y. Palizdar, D. San Martin, M. Ward, R.C. Cochrane, R. Brydson, A.J. Scott, Observation of thermally etched grain boundaries with the FIB/TEM technique, Mater. Charact. 84 (2013) 28–33.
[37] E. Hayward, A. Greenough, The surface energy of solid nickel, J. Inst. Met. 88 (1960) 217–220.
[38] H. Mykura, The variation of the surface tension of nickel with crystallographic orientation, Acta Metall. 9 (1961) 570–576.
[39] T. Williams, P. Barrand, The measurement of the ratio of grain-boundary energy to surface energy as a function of composition, for the copper-nickel system, J. Inst. Met. 93 (1965) 447–449.
[40] P.S. Maiya, J.M. Blakely, Surface self-diffusion and surface energy of nickel, J. Appl. Phys. 38 (1967) 698–704.
[41] L. Murr, O. Inal, G. Wong, Applications of the SEM, TEM and FIM in the analysis of structure and energy of metal interfaces, in: G. Thomas (Ed.), Electron Microscopy and the Structure of Metals, University of California Press, Berkeley (CA), 1972, pp. 417–426.
[42] L. Murr, Interfacial Phenomena in Metals and Alloys, Addison-Wesley Pub. Co., Advanced Book Program, Boston (MA), 1975.
[43] T.A. Roth, The surface and grain boundary energies of iron, cobalt and nickel, Mater. Sci. Eng. 18 (1975) 183–192.
[44] D. Stickle, J. Hirth, G. Meyrick, R. Speiser, A new technique for measuring the effects of oxygen activity on surface energies: application to nickel, Metall. Trans. A 7A (1976) 71–74.
[45] R. Digilov, S. Zadumkin, V. Kumykov, K. Khokonov, Measurement of the surface tension of refractory metals in the solid state, Fiz. Met. Metalloved. 41 (1976) 979–982.
[46] E. Clark, R. Yeske, H. Birnbaum, The effect of hydrogen on the surface energy of nickel, Metall. Trans. A 11A (1980) 1903–1908.
[47] S.V. Divinski, G. Reglitz, G. Wilde, Grain boundary self-diffusion in polycrystalline nickel of different purity levels, Acta Mater. 58 (2010) 386–395.
[48] D. Prokoshkina, V.A. Esin, G. Wilde, S.V. Divinski, Grain boundary width, energy and self-diffusion in nickel: effect of material purity, Acta Mater. 61 (2013) 5188–5197.
[49] Gwyddion Free SPM (AFM, SNOM/NSOM, STM, MFM,...) data analysis software. 01.04.2020, URL http://gwyddion.net/.
[50] J. Schöllhammer, L. Chang, E. Rabkin, B. Baretzky, W. Gust, E. Mittemeijer, Measurement of the profile and the dihedral angle of grain boundary grooves by atomic force microscopy, Z. Metallkd. 90 (1999) 687–690.
[51] Y. Amouyal, E. Rabkin, Y. Mishin, Correlation between grain boundary energy and geometry in Ni-rich NiAl, Acta Mater. 53 (2005) 3795–3805.
[52] H. Ellingham, Reducibility of oxides and sulfides in metallurgical processes, J. Soc. Chem. Ind. 63 (1944) 125–133.
[53] M. Hasegawa, Ellingham diagram, in: S. Seetharaman (Ed.), Treatise on Process Metallurgy, Elsevier, Amsterdam, 2014, pp. 507–516.
[54] V. Randle, Grain boundary planes and their energies as estimated by dihedral angle measurements in nickel, Microsc. Microanal. Microstruct. 4 (1993) 349–358.
[55] C.B. Thomson, V. Randle, A study of twinning in nickel, Scr. Mater. 35 (1996) 385–390.
[56] V. Randle, Relationship between coincidence site lattice, boundary plane indices, and boundary energy in nickel, Mater. Sci. Technol. 15 (1999) 246–252.
[57] V. Randle, P.R. Rios, Y. Hu, Grain growth and twinning in nickel, Scr. Mater. 58 (2008) 130–133.
[58] J. Li, S.J. Dillon, G.S. Rohrer, Relative grain boundary area and energy distributions in nickel, Acta Mater. 57 (2009) 4304–4311.
[59] D.L. Olmsted, S.M. Foiles, E.A. Holm, Survey of computed grain boundary properties in face-centered cubic metals: I. Grain boundary energy, Acta Mater. 57 (2009) 3694–3703.
[60] G.S. Rohrer, E.A. Holm, A.D. Rollett, S.M. Foiles, J. Li, D.L. Olmsted, Comparing calculated and measured grain boundary energies in nickel, Acta Mater. 58 (2010) 5063–5069.
[61] M. Kappeler, A. Marusczyk, B. Ziebarth, Simulation of nickel surfaces using ab-initio and empirical methods, Mater. 12 (2020) 100675.
[62] R. Tran, Z. Xu, B. Radhakrishnan, D. Winston, W. Sun, Surface energies of elemental crystals, Sci. Data 3 (2016) 1–13.
[63] W. Tyson, W. Miller, Surface free energies of solid metals: estimation from liquid surface tension measurements, Surf. Sci. 62 (1977) 267–276.